MnFe layered double hydroxides confined MnO_x for peroxymonosulfate activation: A novel manner for the selective production of singlet oxygen

Hanxuan Zeng[a,b], Bufan Yang[a], Jinchen Zhang[a], Hao Zhu[a], Jing Deng[a,b,*], Zhou Shi[c], Shiqing Zhou[c], Haojie Zhang[d], Anhong Cai[e], Lin Deng[c]

a. College of Civil Engineering, Zhejiang University of Technology, Hangzhou, 310023, PR China

b. Zhejiang Key Laboratory of Civil Engineering Structures & Disaster Prevention and Mitigation Technology, Hangzhou, 310023, PR China

c. Hunan Engineering Research Center of Water Security Technology and Application, Key Laboratory of Building Safety and Energy Efficiency, Ministry of Education, College of Civil Engineering, Hunan University, Changsha, 410082, PR China

d. Department of Environmental Engineering, Helmholtz Centre for Environmental Research-UFZ, Leipzig, 04318, Germany

e. National and Local Joint Engineering Research Center for Ecological Treatment Technology of Urban Water Pollution, College of Life and Environmental Science, Wenzhou University, Wenzhou, 325035, PR China

*Corresponding author.

E-mail addresses: zjut_djing@163.com (J. Deng).

Abstract

Singlet oxygen ($^1O_2$) is a reactive species for the selective degradation of stubborn organic pollutants. Given its resistance to harsh water environment, the effective and exclusive generation of $^1O_2$ is acknowledged as a key strategy to mitigate water production costs and ensure water supply safety. Herein, we synthesized MnO_x intercalated MnFe layered double hydroxides (MF-MnO_x) to selectively produce $^1O_2$ through the activation of PMS. The distinctive confined structure endowed MF-MnO_x with a special pathway for the PMS activation. The direct oxidation of BPA on the intercalated MnO_x induced the charge imbalance in the MnFe-LDH layer, resulting in the selective generation of $^1O_2$. Moreover, acceptable activity deterioration of MF-MnO_x was observed in a 10 h continuous degradation test in actual water, substantiating the application potential of MF-MnO_x. This work presents a novel catalyst for the selective production of $^1O_2$, and evaluates its prospects in the remediation of micro-polluted water.

Keywords: Layered double hydroxides; Confined catalysis; Peroxymonosulfate; Singlet oxygen; Electron transfer process.

1. Introduction

Persulfate activation-based advanced oxidation processes (PS-AOPs) have been confirmed as effective methods for remediating water contaminated with organic pollutants [1]. Through the activation and cleavage of peroxymonosulfate (PMS) and peroxydisulfate (PDS), the generated reactive species (RSs), such as hydroxyl radical (•OH) and sulfate radical ($SO_4^{\bullet-}$), which possess high redox potential can degrade most organic pollutants via radical addition, hydrogen atom abstraction, and single electron transfer [2]. However, the presence of coexisting ions and natural organic matters (NOMs) in natural water may competitively quench the radicals, resulting in lower-than-expected treatment efficiency [3]. Therefore, nonradical pathway-based PS-AOPs, characterized by insensitivity to environmental factors and high oxidant utilization efficiency, has garnered attention from researchers [4, 5].

Heterogeneous PS activation is regarded as one of the most flexible approaches to introduce nonradical mechanism to PS-AOPs [6, 7]. In comparison with the radical dominated cobalt ion-activated PMS system, cobalt single atom catalysts prepared with chitosan as the precursor not only activate PMS to produce more radicals but also introduce nonradical pathways to the degradation of carbamazepine [8]. Nevertheless, the production of radicals susceptible to the water matrix still increases the consumption of PS. Thus, the targeted activation of PS has become the current research trend. Singlet oxygen ($^1O_2$), one of the three mainstream nonradical pathways ($^1O_2$, high valence metal (HVM) and electron transfer process (ETP)), is the most widely studied nonradical pathway that can selectively produce [6, 9]. Compared with radicals, $^1O_2$, with a suitable redox potential of 2.2 V,

possesses high selectivity to the electron-rich organic pollutants, and can efficiently remove pollutants that play important roles in PS-AOPs [10, 11]. The generation of $^1O_2$ with nearly 100% selectivity was achieved by PMS activation using carbon nitride supported high loading Fe single atom and single atom copper embedded MXene as the catalysts [12, 13]. Through suppressing the spontaneous dissociation of adsorbed PMS on the single atom CoN_{2+2} active sites, the exclusive generation of $^1O_2$ via nonradical pathways was achieved [14].

However, the current challenge is that the targeted activation of PS can almost only be achieved by using single atom catalysts, whereas the PS activation by widespread metal oxides/hydroxides with milder synthesis conditions is unpredictable, and the mixed mechanism of radical and nonradical is more common [15, 16]. The basis for designing high selectivity catalysts is to first elaborate on the mechanism of the $^1O_2$ production. Briefly, the bonding of PS molecule to the surface active sites of the catalyst is the first step in the PS activation. Therein, the transfer of electron from the catalyst to PS would cleave the peroxy bond of PS molecules and produce radicals [17]. For the $^1O_2$ nonradical pathway, this process may be reversed, where electron transfer from PS to its bonded active site leads to the production of $^1O_2$ [13]. It should be noted that HVM and ETP can also be produced from the spontaneous decomposition of PS via electron shuttle, which depends on the redox potential of PS bonded with the active site of the catalyst [18, 19].

Based on the above, we synthesized MnO_x intercalated MnFe layered double hydroxides (MF-MnO_x) using a confined encapsulation strategy to activate PMS for the selective

85 production of $^1O_2$. In this work, the confined structure of MF-MnO_x was determined through
86 several characterization and deliberately designed experiments. The catalytic performance of
87 MF-MnO_x was evaluated using Bisphenol A (BPA) as the model pollutant. Specifically,
88 although some experimental phenomena deliberately pointed to ETP as the dominant
89 mechanism of the BPA degradation, we still lifted the cloud of uncertainty hanging over the
90 catalytic mechanism and first proposed the selective generation of $^1O_2$ induced by the passive
91 charge imbalance in the catalyst. This work demonstrates a manner for the selective
92 production of $^1O_2$ by activating PMS with metal oxide/hydroxide.

93 **2. Materials and methods**

94 *2.1. Chemicals*

95 Potassium peroxymonosulfate was acquired from Sigma-Aldrich®, and other reagents
96 were purchased from Sinopharm Chemical Reagent Co., Ltd., China. All reagents were
97 analytical grade and used as received without further purification. Ultrapure water was used
98 in all experiments.

99 *2.2. Synthesis of MF-MnO_x*

100 CaFe-LDH was first synthesized as the precursor of MF-MnO_x. Briefly, $Ca(NO_3)_2{\cdot}4H_2O$
101 and $Fe(NO_3)_3{\cdot}9H_2O$ were dissolved in 200 mL of ultrapure water with molar ratio of 2:1, 3:1
102 and 4:1. Then, the alkaline liquor was prepared by dissolving quantitative NaOH (C_{OH^-} =
103 $C_{Ca2++Fe3+}\times C_{Ca2+/Fe3+}$) in another 200 mL of ultrapure water. Subsequently, the mixed metal
104 salt solution was dropwise added to the NaOH solution with vigorous stirring under nitrogen
105 atmosphere. Whereafter, the suspension was aged at 60 ℃ for 10 h to obtain CaFe-LDH.

CaFe-LDH with different Ca/Fe molar ratios were named C_2F_1-LDH, C_3F_1-LDH and C_4F_1-LDH, respectively.

As described in Fig. S1, 2g of CaFe-LDH was immersed in 200 mL of $KMnO_4$ solution (0.004 M) with vigorous stirring under nitrogen atmosphere for 12 h to gain MnO_4^- intercalated CaFe-LDH. After filtration and washing with ultrapure water, the obtained filter cake was redispersed in 100 mL of $MnCl_2$ solution (0.012 M) with vigorous stirring at 40 ℃ for 12 h. Finally, the black product was collected, washed and dried at 70 ℃ to acquire MF-MnO_x. Similarly, MF-MnO_x derived from different CaFe-LDH samples were labeled as M_2F_1-MnO_x, M_3F_1-MnO_x and M_4F_1-MnO_x, respectively. The samples derived from CaAl-LDH through the same synthetic method was named MA-MnO_x, and the samples obtained by immersing CaFe-LDH without MnO_4^- in $MnCl_2$ solution was named MF-LDH.

Characterization, experimental and analytic methods are provided in Texts S1-S3 and Tab. S1 in Supporting Information.

3. Results and discussion

3.1. Catalysts characterization

The phase composition of MF-MnO_x was determined using XRD. As displayed in Fig. S2a, the peaks at 2θ = 31.3° can be indexed to the (104) lattice planes of MnFe-LDH [20, 21]. Significantly, none of the characteristic peaks representing CaFe-LDH (Fig. S2b) were found in MF-MnO_x. This suggests that CaFe-LDH was completely transformed into MnFe-LDH with isomorphous substitution of Ca^{2+} by Mn^{2+} in the LDH structure [22]. Moreover, peaks related to the (112), (103) and (211) crystal planes of MnO_x were detected at 2θ = 29.2°,

32.5° and 36.1° [23, 24]. The formation of MnO_x can be deciphered by the simultaneous comproportionation reaction between Mn^{2+} and intercalated MnO_4^- during the isomorphous substitution process. Furthermore, the intensity of the characteristic peaks of MF-MnO_x varied with the Ca/Fe molar ratio. Briefly, the intensity of the (104) crystal plane representing MnFe-LDH enhanced with the increase in the Ca ratio, while the peak associated with MnO_x gradually decreased. A possible explanation for this can be that CaFe-LDH with a high content of Ca possessed a lower exchange capacity for MnO_4^-, leading to the increased formation of MnFe-LDH and the reduced production of MnO_x [25, 26].

The surface morphology of MF-MnO_x was characterized by SEM. As shown in Fig. 1a, MF-MnO_x possessed a typical lamellar structure of brucite, suggesting that mild synthesis condition would not result in the collapse of the LDH structure. On the other hand, this implies that MnO_x might intercalate in the interlayer of MnFe-LDH, rather than simply loading on the surface of MnFe-LDH. As seen, the standing-up nanosheets of MF-MnO_x with a mean size of 200 nm were found in the HR-TEM image (Fig. 1b). The result further verifies the fact that MnO_x intercalated in the interlayer of MnFe-LDH. EDS-mapping of MF-MnO_x demonstrates that the as-prepared catalyst was formed by uniformly distributed Fe, Mn and O elements (Fig. 1c). Moreover, as shown in Fig. 1d, the content of Ca in MF-MnO_x was less than 1 wt%, which can be ignored.

3.2. Catalytic performance assessment

The catalytic activity of MF-MnO_x was evaluated using BPA as the targeted pollutant. As shown in Fig. 2a, the direct oxidation of BPA by PMS can be ignored, suggesting the

148 reactionlessness of PMS without the presence of catalyst. Additionally, the adsorption of BPA
149 by M_2F_1-MnO_x was also excluded. The precursor CaFe-LDH possessed limited promotion on
150 the PMS activation, while only 35.6% of BPA was diluted by the CaFe-LDH/PMS system
151 within 20 min reaction time. As for MF-MnO_x, it is evident that the catalytic performance
152 varied significantly with different Ca/Fe molar ratio precursors. The removal of BPA by the
153 M_2F_1-MnO_x/PMS, M_3F_1-MnO_x/PMS and M_4F_1-MnO_x/PMS systems were 99.7%, 71.1% and
154 64.0% with the reaction time of 15 min. It is worth noting that, except for the
155 M_2F_1-MnO_x/PMS system, the fitting degree of the BPA degradation to the first-order kinetic
156 model was low in other systems (Fig. S3). Especially for the samples derived from the
157 precursor with a high content of Ca, two oxidation stages were found in the BPA degradation
158 process. This should be associated with the low content of MnO_x in M_3F_1-MnO_x and
159 M_4F_1-MnO_x. The reaction between PMS and MnO_x in the interlayer of MnFe-LDH relied on
160 the contact of PMS with enough active sites during the mass transfer process [27, 28]. The
161 lack of MnO_x induced the delayed degradation of BPA in the M_3F_1-MnO_x/PMS and
162 M_4F_1-MnO_x/PMS systems. Therefore, unless otherwise specified, M_2F_1-MnO_x was chosen as
163 the research object and abbreviated as MF-MnO_x. The mineralization rate of BPA was
164 measured by TOC analysis. From Fig. S4, 99.7% of BPA can be attenuated while the TOC
165 removal was 55.2% within 20 min. Prolonging the reaction time to 30 min, it can be seen that
166 81.6% of TOC removal was achieved, suggesting the sustainable degradation capacity of the
167 MF-MnO_x/PMS system.

168 The effect of reaction temperature on the BPA degradation by the MF-MnO_x/PMS

system was investigated to determine the controlling factor of the catalytic reaction [29]. Fig. 2b exhibits the BPA removal at 15 ℃, 25 ℃ and 35 ℃, elevated temperature was found to be beneficial to the BPA attenuation, and the reaction rate constants (k_{obs}) were calculated to be 0.11, 0.21 and 0.31 min^{-1} at reaction temperature of 15 ℃, 25 ℃ and 35 ℃, respectively. The inserted figure in Fig. 2b shows a linear relationship between ln(k_{obs}) and the reciprocal of the reaction temperature (1/T), hence, the activation energy (E_a) for the BPA degradation was estimated as 37.9 kJ/mol through the Arrhenius equation [30]. This value exceeds the range of 10-13 kJ/mol attributed to diffusion-controlled reactions, implying that the catalytic reaction was controlled by surface chemical reaction instead of mass transfer [31]. The above results also indicate that the MnO_x load was sufficient to achieve the instantaneous PMS activation.

3.3. Reactive species (RSs) identification

Radical ($SO_4^{\bullet-}$, $^{\bullet}OH$) and nonradical ($^1O_2$, HVM, ETP) pathways are commonly recognized in the PMS activation process [1, 6]. Especially in heterogeneous catalysis, the coexistence of multiple pathways is always more common than single catalytic mechanism. Thus, the possible RSs and oxidation processes in the MF-MnO_x/PMS system were carefully determined by elaborate experiments and characterization. Firstly, ESR was carried out to directly detect the produced radicals. As displayed in Fig. 3a, misleading DMPOX adducts were found when DMPO was used as the spin trap compound. These may refer to deeply oxidized DMPO-$SO_4^{\bullet-}$ and DMPO-$^{\bullet}OH$ adducts or non-radical pathways, including HVM and $^1O_2$ [19]. The ambiguous information compelled us to conduct further investigation to

verify the existence of free radicals. The six characteristic peaks of DMPO-$O_2^{\bullet-}$ and the triplet signals of TEMP-$^1O_2$, as shown in Fig. 3b and c, suggest the yield of $O_2^{\bullet-}$ and $^1O_2$ in the MF-MnO_x/PMS system [32]. Then, different RSs and oxidation processes and their contribution to the BPA degradation are discussed in detail in the following sections.

3.3.1. Free radicals

Comparative experiments were performed using nitrobenzene (NB), benzoic acid (BA) and atrazine (ATZ) as the probes. NB is known to be insensitive to RSs except $^{\bullet}OH$ ($k_{[NB,\bullet OH]}$ = 3.9×10^9 M^{-1} s^{-1}), while BA and ATZ, with electron-deficient structure, preferentially react with $^{\bullet}OH$ and $SO_4^{\bullet-}$ ($k_{[BA,\bullet OH]}$ = 3.9×10^9 M^{-1} s^{-1}, $k_{[BA,\ SO4\bullet-]}$ = 1.2×10^9 M^{-1} s^{-1}, $k_{[ATZ,\bullet OH]}$ = 2.3×10^9 M^{-1} s^{-1}, $k_{[ATZ,SO4\bullet-]}$ = 2.6×10^9 M^{-1} s^{-1}) [33]. As exhibited in Fig. 3d, NB and BA were stubborn in the MF-MnO_x/PMS system, with less than 10% of NB and BA were eliminated within 20 min reaction time. This indicates the negligible contribution of $^{\bullet}OH$ and $SO_4^{\bullet-}$ to the BPA degradation. Surprisingly, the removal of ATZ, with similar properties to BA, reached 20% under the same conditions. Therefore, the adsorption of ATZ by MF-MnO_x was tested, as shown in Fig. S5a, ATZ reached ad/desorption equilibrium in a very short time, and nearly 50% of ATZ was enriched from the water phase to the catalyst surface. The result provides a crucial clue that competitive occupation of active sites between PMS and pollutants might occur on the catalyst surface, potentially affecting ETP induced by the co-occupation of PMS and BPA at the solid-liquid interface [34].

3.3.2. Singlet oxygen and superoxide radical

1,4 benzoquinone (BQ) possesses selective trap capability for $O_2^{\bullet-}$ ($k_{[BQ,O2\bullet-]}$ =

211 0.9-1.0×10^8 M^{-1} s^{-1}) [35, 36]. Relying on the high reactivity of furfuryl alcohol (FFA) toward
212 $^{\bullet}OH$ and $^1O_2$ ($k_{[FFA,\ ^{\bullet}OH]}$ = 1.5×10^{10} M^{-1} s^{-1}), $k_{[FFA,1O2]}$ = 1.2×10^8 M^{-1} s^{-1}), FFA was employed to
213 identify the actual contribution of $^1O_2$ to the BPA removal [37, 38]. As depicted in Fig. S5b,
214 with 1 mM BQ and 10 mM FFA addition, the BPA removal declined to 86.1% and 64.5%,
215 and the corresponding k_{obs} values decreased to 0.08 and 0.05 min^{-1}, implying the participation
216 of $O_2^{\bullet-}$ and $^1O_2$. Considering that the direct consumption of PMS by FFA may lead to
217 misleading conclusions, the degradation of BPA by the MF-MnO_x/PMS system was
218 conducted using D_2O instead of H_2O as the solvent [39]. The higher lifetime of $^1O_2$ in D_2O
219 endows it with more active oxidation ability [40]. As illustrated in Fig. S6, the BPA
220 degradation in D_2O was markedly elevated, with the k_{obs} value increased from 0.21 to 0.26
221 min^{-1}, suggesting the crucial role of $^1O_2$ in the BPA removal. For $O_2^{\bullet-}$ with a negative redox
222 potential (-0.8 V), the direct oxidation of BPA by $O_2^{\bullet-}$ was insignificant [40]. Therefore, the
223 inhibition of the BPA degradation induced by scavenging $O_2^{\bullet-}$ deserves investigation. Oxygen
224 circulation is the link between $O_2^{\bullet-}$ and $^1O_2$, if the BPA degradation is suppressed in an
225 oxygen-free environment, then $O_2^{\bullet-}$ should be the important precursors of $^1O_2$ [35]. As shown
226 in Fig. S6, the k_{obs} value of the BPA degradation in a nitrogen saturation situation was only
227 0.08 min^{-1}, confirming the origin of $^1O_2$. Notably, the BPA removal in an anaerobic
228 environment still reached 84.5%, indicating that $^1O_2$ might not be the dominant RSs.

229 *3.3.3. High valence metal (HVM)*

230 HVM with strong oxidizing has been verified as a typical nonradical pathway in
231 previous studies [7]. Thus, methyl phenyl sulfoxide (PMSO) was used to detect the generated

high valence iron and manganese [41]. As depicted in Fig. S7, Compared with the sole PMS system, the addition of MF-MnO_x did not promote the removal of PMSO and the formation of $PMSO_2$. This result indeed excludes the participation of HVM in the BPA degradation.

3.3.4. Direct oxidation process (DOP) and electron transfer process (ETP)

Acidic PMS can trigger MnO_x to oxidize organic contaminants through DOP [42]. The pH fluctuation during the reaction was recorded using a hypersensitive pH meter. As tested, the solution pH instantaneously declined to 3.88 with PMS addition and stabilized within plus or minus 0.2 in the follow-up degradation process. Hence, the contribution of DOP was simulated by maintaining the solution pH at 3.88 using 0.1 M H_2SO_4. As shown in Fig. 4a, 36.4% of BPA was eliminated by DOP within reaction time of 20 min, implying the significance of the BPA oxidation induced by acidity. More importantly, the BPA degradation poorly fitted the first-order kinetic model, but the reaction rate increased with prolonging the reaction time. A credible explanation for this is that the confined space of MnFe-LDH buffered the change in the surface chemistry micro-environment of the intercalated MnO_x and delayed the acidity-induced oxidation [43].

The electron transfer between PMS and BPA induced by catalyst as electron shuttle is a noteworthy nonradical degradation mechanism [6]. Firstly, the premixing experiment was operated to confirm ETP. As shown in Fig. 4b, the premixing of MF-MnO_x and PMS promoted the BPA degradation in the early stage of the reaction, which might be related to the advance of DOP. The mass transfer of PMS in the interlayer of MnFe-LDH was completed during the premixing process, and BPA can be degraded immediately by acid-activated MnO_x.

However, the premature mixing of PMS with MF-MnO_x resulted in the slight inhibition of the BPA degradation in the later stage of the reaction. This might be due to the self-quenching of the produced $^1O_2$ during the premixing process. The above results indeed imply that ETP, not controlled by premixing time, may be the dominant mechanism. Significantly, the suppression of the BPA degradation did not enhance with prolonging the premixing time, which differed from previous reports [44]. This may be related to the generation and self-quenching of $^1O_2$ at nearly equal rate in the absence of BPA.

Open-circuit potential analysis was performed to identify the existence of ETP. As displayed in Fig. 4c, the addition of PMS elevated the MF-MnO_x potential from ~0.33 to ~0.37 V, indicating the formation of high-energy metastable intermediates [6]. Surprisingly, the involvement of BPA did not reduce the potential of MF-MnO_x as reported in previous literature. For one thing, the redox potential of the metastable intermediates formed by MF-MnO_x and PMS was low and insufficient to capture electron from BPA [45]. For another, the competitive occupation of active sites between PMS and BPA blocked the electronic channel from BPA to PMS via catalyst. The PMS consumption in the MF-MnO_x/PMS system with/without BPA presence was further monitored to exclude ETP between BPA and MF-MnO_x-PMS intermediates. As seen in Fig. 4d, the addition of BPA hardly effected the PMS decomposition, reliably supporting the conclusion obtained from the open-circuit potential analysis [46].

3.4. Catalytic mechanisms analysis

Although the aforementioned discussion verifies the secondary role of $^1O_2$ and DOP in

the BPA degradation, the dominant mechanism has been proven not to be ETP, leaving us with difficulties. Therefore, there is a possibility that $^1O_2$ and DOP did not exist independently but cooperatively, to this end, ingenious experiments were designed to prove this conjecture.

3.4.1 Origin of $^1O_2$

Typically, dissolved oxygen and PMS molecule are considered as the main precursors of $^1O_2$. Of which, the $^1O_2$ production from O_2 via $O_2^{\bullet-}$ and PMS via $SO_5^{\bullet-}$ are recognized reaction pathways [40, 47]. Although the discussion in section 3.3.2 confirmed the $^1O_2$ evolution pathway involving O_2 and $O_2^{\bullet-}$, the generation of $^1O_2$ from PMS cannot be ruled out. Thus, quantitative ESR was performed to identify the origin of $^1O_2$. As shown in Fig. 5a and Tab. S2, the yield of $^1O_2$ in the MF-MnO_x/PMS system in ultrapure water was determined to be 2.72×10^{11} spins/mm^3 using the spins per unit volume as the index. However, with the addition of 1 mM BQ, the generation of $^1O_2$ declined to 1.95×10^{11} spins/mm^3, suggesting the uniqueness of the precursor of $^1O_2$ without BPA presence. Surprisingly, different from the general cognition, instead of suppressing the intensity of TEMP-$^1O_2$, the addition of BPA greatly increased the generation of $^1O_2$ (3.45×10^{11} spins/mm^3), indicating that DOP can synergistically promote the $^1O_2$ production while degrading BPA. Further confirmation of the effect of BQ on the yield of $^1O_2$ with BPA involvement showed that the addition of 1 mM BQ reduced the $^1O_2$ production of 0.86×10^{11} spins/mm^3, equivalent to the $^1O_2$ yield from $O_2^{\bullet-}$ in the MF-MnO_x/PMS system in ultrapure water. This result implies that instead of promoting the conversion of $O_2^{\bullet-}$ to $^1O_2$, DOP triggered the generation pathway of $^1O_2$ from PMS

295 molecule.

296 *3.4.2 Evolution of $^1O_2$ from PMS*

297 As mentioned in section 3.3.4, open-circuit potential analysis identified the generation of
298 the high-energy metastable MF-MnO_x-PMS intermediates. Although MF-MnO_x-PMS cannot
299 directly degrade BPA through ETP, the decomposition of the intermediates could result in the
300 generation of $^1O_2$ through the biradical reaction between two $SO_5^{\bullet-}$ (Eqs. 1-2) [47]. This
301 process would not reduce the open-circuit potential of MF-MnO_x but generate PDS in situ,
302 leading to the confused result of the PMS decomposition (PDS possesses the same absorption
303 wavelength as PMS; 415 nm) [48].

304 $$M^{n+1}\text{-}HSO_5^- \rightarrow M^n\text{-}SO_5^{\bullet-} + H^+ \quad (1)$$

305 $$2M^n\text{-}SO_5^{\bullet-} \rightarrow M^n\text{-}S_2O_8^{2-}\text{-}M^n + {}^1O_2 \quad (2)$$

306 For this case, in situ-Raman was operated to confirm this process. As shown in Fig. 5b,
307 the peaks at 980 and 1086 cm^{-1} can be indexed to SO_4^{2-} and the metastable MF-MnO_x-PMS
308 intermediates, suggesting the reaction between MF-MnO_x and PMS [45]. Whereafter, the
309 addition of BPA led to the blue shift of the peak representing metastable intermediates from
310 1086 to 1006 cm^{-1}. It is reasonable to presume that the new peak can be attributed to the
311 MF-MnO_x-PDS-MF-MnO_x intermediates, which was generated simultaneously with the $^1O_2$
312 production by PMS via $SO_5^{\bullet-}$ [47]. Significantly, MF-MnO_x was inert to the PDS activation
313 (Fig. S8), indicating that MF-MnO_x-PDS-MF-MnO_x might possess a lower redox potential
314 than MF-MnO_x-PMS. It also suggests that the generation of MF-MnO_x-PDS-MF-MnO_x from
315 MF-MnO_x-PMS was thermodynamically feasible.

316 *3.4.3 Active site identification*

317 So far, the synergy between the catalytic mechanisms has been clarified, and the only
318 remaining puzzle is the relationship between DOP and the cleavage of MF-MnO_x-PMS.
319 Considering the electron transfer from PMS to MF-MnO_x was the initial step to produce
320 $SO_5^{\bullet-}$, the active sites of MF-MnO_x were first identified. XPS was performed to reveal the
321 element valence change of MF-MnO_x during the catalytic reaction (Fig. 6 and Tab. S3). From
322 Fig. 6a, the peaks at 644.8, 640.9 and 640.6 eV were related to Mn(IV), Mn(III) and Mn(II),
323 respectively [49]. After the reaction, the relative content of the three valence of manganese
324 changed from 19.8%, 60.9% and 19.3% to 16.2%, 71.5% and 12.3%, respectively. With
325 regard to DOP induced by the intercalated MnO_x, Mn(IV) could capture an electron from
326 BPA leading to the BPA degradation and the increase of Mn(III) [42]. Then, BPA can be
327 further degraded along with the reduction of Mn(III) to Mn(II) [42]. However, from the XPS
328 Mn 2p spectrum, the relative content of Mn(II) declined instead of increasing. Therefore, the
329 change in different valence of manganese was further accurately demonstrated by the XPS
330 Mn 3s spectrum. As depicted in Fig. 6b, the ΔE value MF-MnO_x declined from 6.2 to 6.0 eV,
331 suggesting that the overall valence of manganese elevated after the reaction, and the
332 oxidation of Mn(II) to Mn(III) far exceeded the conversion of Mn(III) to Mn(II) [50]. This
333 can be accounted for by the special bimetallic structure of MnFe-LDH, in which bimetallic
334 atoms bonded to the same oxygen atom can undergo a redox cycle by charge balance [51].
335 This point is verified by the XPS Fe 2p spectrum (Fig. 6c), where peaks at 711.6 and 709.7
336 eV can be classified as Fe(III) and Fe(II), respectively. The catalytic reaction resulted in the

reduction of 17.1% of Fe(III) to Fe(II). Hence, the catalytic sites of MF-MnO_x for the PMS activation should be Fe(III), which was reduced to Fe(II) by capturing electrons from BPA. The XPS O 1s spectrum further reveals the bonding between Fe(III) sites and PMS molecule. As seen in Fig. 6d, the XPS O 1s spectrum can be deconvoluted into water molecule (O_W), lattice hydroxyl (O_{OH}), lattice oxygen (O_L) and adsorbed oxygen (O_O) [35]. Of which, the decrease of O_O in the used MF-MnO_x confirms the generation of $^1O_2$ from O_2. More importantly, 7.2% of O_{OH} transformed into other O species, suggesting that Fe(III)-OH provided ideal coordinating sites for PMS to form the inner-sphere metastable intermediates (Fe(III)-SO_3OOH) via the displacement of surface hydroxyl groups (Eq. 3) [50]. Since $H_2PO_4^-$ can compete with PMS for Fe(III)-OH active sites, the key role of Fe(III)-SO_3OOH was further demonstrated by adding $H_2PO_4^-$ into the BPA solution [35]. As illustrated in Fig. S9, the strong inhibition of $H_2PO_4^-$ on the BPA degradation by the MF-MnO_x/PMS system indeed verifies the absolute necessity of Fe(III)-SO_3OOH in the PMS activation.

$$\text{Fe(III)-OH} + HSO_5^- \rightarrow \text{Fe(III)-}SO_3OOH + OH^- \quad (3)$$

3.4.4 Mechanism of PMS activation

To sum up, the PMS activation by MF-MnO_x is illustrated in Fig. 7, Fe(III)-OH on the MF-MnO_x surface instantly bond with PMS to form Fe(III)-SO_3OOH through the displacement of surface hydroxyl groups (Eq. 3) [50]. However, the redox potential of Fe(III)-SO_3OOH was insufficient to directly degrade BPA. Meanwhile, DOP induced by the confined MF-MnO_x is slightly delayed due to the buffering of the MnFe-LDH layer. Once the mass transfer of PMS in the interlayer of MnFe-LDH is completed, the intercalated MnO_x

could degrade BPA along with the reduction of Mn(IV)/Mn(III) to Mn(II) via DOP [52]. The charge imbalance in the MnFe-LDH layer triggered by excess Mn(II) in MnO_x through the metal-oxygen bond could result in the electron transfer from the bonded PMS to Fe(III) active sites. Surface-bond $SO_5^{\bullet-}$ generated in the process would promote the production of PDS and $^1O_2$ via biradical reaction (Eqs. 4-5) [47].

$$Fe(III)\text{-}SO_3OOH \rightarrow Fe(III)\text{-}SO_5^{\bullet-} + H^+ \quad (4)$$

$$2Fe(III)\text{-}SO_5^{\bullet-} \rightarrow Fe(II)\text{-}S_2O_8^{2-}\text{-}Fe(II) + {}^1O_2 \quad (5)$$

To further confirm the synergism of DOP and the $^1O_2$ generation, we evaluated the catalytic performance of MA-MnO_x and MF-LDH. As shown in Fig. S10, the k_{obs} values of the MA-MnO_x/PMS and MF-LDH/PMS systems were calculated as 0.02 min and 0.03 min^{-1}, suggesting that the efficient degradation of BPA depended on the simultaneous presence of Fe(III) active site and MnO_x. Moreover, the synergic coefficient (ξ) of Fe(III) active site and MnO_x was determined via Eq. 6 [53]. As calculated, the ξ value was 4.2, definitely verifying the promotion of the $^1O_2$ production by DOP.

$$\xi = k_{obs}(\text{MF-}MnO_x\text{/PMS})/(k_{obs}(\text{MA-}MnO_x\text{/PMS})+k_{obs}(\text{MF-LDH/PMS})) \quad (6)$$

In summary, DOP, $^1O_2$ from PMS activation inspired by DOP and $^1O_2$ produced from O_2 were jointly responsible for the BPA degradation.

3.5. Effect of key parameters

Effect of the solution initial pH on the BPA degradation by the MF-MnO_x/PMS system was investigated. As depicted in Fig. 8a and Fig. S11a, the k_{obs} values of pH at 3.0, 5.0, 7.0 and 9.0 were 0.11, 0.12, 0.22 and 0.18 min^{-1}, respectively. The variation in environmental

adaptability of DOP and $^1O_2$ in the solution explains this trend. DOP prefers to oxidize BPA under acidic condition, whereas $^1O_2$ is more active in alkaline solution [54]. Although adjusting the solution pH inhibited the BPA degradation, the BPA removal remained above 90% within the pH range of 3.0 to 9.0, suggesting the outstanding performance of the MF-MnO_x/PMS system over a wide pH range. In comparison to radical-based systems sensitive to pH, the MF-MnO_x/PMS system exhibits greater promise for the treatment of micro-polluted water.

The effect of coexisting anions on the BPA degradation was studied, with Cl^-, CO_3^{2-} and NO_3^- as the objects. As shown in Fig. 8b and Fig. S11, with concentration of Cl^-, CO_3^{2-} and NO_3^- increasing from 1 to 100 mM, the BPA removal by the MF-MnO_x/PMS system consistently exceeded 90%, implying the insensitiveness of the catalytic system to the environmental factors. Furthermore, the degradation efficiency of BPA was highly dependent on the type and concentration of coexisting anions, especially those affecting catalyst surface properties and reacting with PMS, rendering the process more unpredictable [50]. Overall, the substantial influence of environmental factors on the catalytic process with multi-mechanism deserves more attention.

As one of the most common substances in natural water, the effect of humic acid (HA) on the BPA degradation was also performed. As depicted in Fig. S12, the existence of 1, 5, 10 mg/L HA suppressed the BPA removal to 58.5%, 67.1% and 73.8%. This can be explained by the competitive consumption of $^1O_2$ by HA, leading to the decrease of effective RSs. Significantly, increased concentration of HA did not actually lead to more disastrous

inhibition of the BPA degradation. This can be attributed to the fact that HA with electron-rich structure can promote the production of $^1O_2$ [55].

3.6. Durability of MF-MnO_x in actual water treatment

Since the deterioration of catalytic performance over extended use is a critical concern for practical catalyst application, the cycling stability of the catalyst was examined. Given the difficulty of recovering powder catalysts, we constructed a self-developed fixed-bed reactor, in which MF-MnO_x was encapsulated in a polymethyl methacrylate tube with quartz wool (Fig. S13a). The mixed solution of PMS and BPA, prepared with Qiantang River water (Tab. S4), was continuously pumped into the reactor through a peristaltic pump and then returned to the beaker to achieve continuous-flow. As shown in Fig. S13b, the BPA removal maintained 100% in the first 6 h, and gradually declined to 72.4% after 10 h of continuous operation, suggesting the superior stability of MF-MnO_x. The slight deterioration of MF-MnO_x might be attributed to the gradual loss of active sites during long-term use. Therefore, the concentration of metal ions leaking from the catalyst was monitored during each cycle. From Fig. S13b, the dissolution of metal ions from MF-MnO_x decreased gradually with prolonging the operation time, and the peak values of Fe ions and Mn ions were 0.16 mg/L and 0.07 mg/L, respectively, lower than the drinking water standard of China (0.3 mg/L for Fe and 0.1 mg/L for Mn). This implies that MF-MnO_x might be an eco-friendly catalyst for the PMS activation.

3.7. Degradation pathway

The degradation intermediates of BPA in the MF-MnO_x/PMS system were analyzed by

the liquid chromatography and mass spectroscopy-MS/MS. As shown in Figure S14a, BPA and six degradation products can be found in the solution. Then, the degradation pathway of BPA was proposed based on the m/z of the degradation intermediates (Figure S14b). According to the catalytic mechanisms analysis, BPA can be degraded by two oxidation processes, including DOP and $^1O_2$. For the DOP route, an electron transferred from BPA to MF-MnO_x would lead to the formation of BPA radical, then, unstable BPA radical would rapidly split into P1 and P2 through homolytic reaction [42]. Meanwhile, P1 and P2 tended to repolymerize to P3 during the electron transfer process [45]. With regards to the $^1O_2$ route, under the attack of $^1O_2$, the aldehydes and hydroxylation reaction occurred on the benzene ring of BPA leading to the formation P4, then, P4 would be further oxidated by $^1O_2$ to produce P5 and P6 [56]. Finally, BPA could be gradually mineralized into inorganic molecules.

4. Conclusion

Selective production of $^1O_2$ from the PMS activation using low-cost metal oxides/hydroxides as the catalyst was realized in this work, providing deep insights into the design of highly selective catalysts. The MF-MnO_x/PMS system exhibited outstanding performance, with the BPA removal exceeding 99% within 20 min. The PMS activation by MF-MnO_x was purely dominated by nonradical pathway, and the BPA degradation was attributed to DOP and its inductively produced $^1O_2$. The unique confined structure of MF-MnO_x was proven to be the key to the special catalytic mechanism, in which the direct oxidation of BPA on the intercalated MnO_x induced the charge imbalance in the MnFe-LDH

layer, and the reverse transfer of electron from the bonded PMS to the catalyst led to the selective production of $^1O_2$. The MF-MnO_x/PMS system possessed strong resistance to harsh water environment, which is a promising strategy for the remediation of micro-polluted water.

Conflicts of interest

The authors declare no conflict of interest.

Acknowledgments

This work was supported by National Natural Science Foundation of China (Grant No. 52300014, 52270004 and 51978618), Zhejiang Provincial Natural Science Foundation of China (Grant No. LQ24E080020 and LZ24E080005), The Science & Technology Innovation Program of Hunan Province (Grant No. 2021RC3039), and Natural Science Foundation of Hunan Province (Grant No. 2021JJ40069). The authors would like to thank Shiyanjia Lab (www.shiyanjia.com) for the XPS analysis.

References

[1] G.P. Anipsitakis, D.D. Dionysiou, Radical Generation by the Interaction of Transition Metals with Common Oxidants, Environmental Science & Technology, 38 (2004) 3705-3712.

[2] R. Xiao, T. Ye, Z. Wei, S. Luo, Z. Yang, R. Spinney, Quantitative Structure–Activity Relationship (QSAR) for the Oxidation of Trace Organic Contaminants by Sulfate Radical, Environmental Science & Technology, 49 (2015) 13394-13402.

[3] J.E. Grebel, J.J. Pignatello, W.A. Mitch, Effect of Halide Ions and Carbonates on Organic Contaminant Degradation by Hydroxyl Radical-Based Advanced Oxidation Processes in Saline Waters, Environmental Science & Technology, 44 (2010) 6822-6828.

[4] A. Jawad, K. Zhan, H. Wang, A. Shahzad, Z. Zeng, J. Wang, X. Zhou, H. Ullah, Z. Chen, Z. Chen, Tuning of Persulfate Activation from a Free Radical to a Nonradical Pathway through the Incorporation of Non-Redox Magnesium Oxide, Environmental Science & Technology, 54 (2020) 2476-2488.

[5] J. Lee, U. von Gunten, J.-H. Kim, Persulfate-Based Advanced Oxidation: Critical Assessment of Opportunities and Roadblocks, Environmental Science & Technology, 54

(2020) 3064-3081.
[6] W. Ren, C. Cheng, P. Shao, X. Luo, H. Zhang, S. Wang, X. Duan, Origins of Electron-Transfer Regime in Persulfate-Based Nonradical Oxidation Processes, Environmental Science & Technology, 56 (2022) 78-97.
[7] Y. Zong, X. Guan, J. Xu, Y. Feng, Y. Mao, L. Xu, H. Chu, D. Wu, Unraveling the Overlooked Involvement of High-Valent Cobalt-Oxo Species Generated from the Cobalt(II)-Activated Peroxymonosulfate Process, Environmental Science & Technology, 54 (2020) 16231-16239.
[8] D. Wang, L. Wang, G. Liang, H. Li, Z. Liu, Z. Tang, J. Liang, C. Zhi, A Superior δ-MnO_2 Cathode and a Self-Healing Zn-δ-MnO_2 Battery, ACS Nano, 13 (2019) 10643-10652.
[9] X. Guo, Q. Zhang, H. He, A. Cai, S. Xi, J. Du, F. Zhang, X. Fan, W. Peng, Y. Li, Wastewater flocculation substrate derived three-dimensional ordered macroporous Co single-atom catalyst for singlet oxygen-dominated peroxymonosulfate activation, Applied Catalysis B: Environmental, 335 (2023) 122886.
[10] C. Guo, C. Tao, F. Yu, Z. Zhao, Z. Wang, N. Deng, X. Huang, Ball-milled layer double hydroxide as persulfate activator for efficient degradation of organic: Alkaline sites-triggered non-radical mechanism, Journal of Hazardous Materials, 461 (2024) 132219.
[11] L. Liu, Y. Li, W. Li, R. Zhong, Y. Lan, J. Guo, The efficient degradation of sulfisoxazole by singlet oxygen ($^1O_2$) derived from activated peroxymonosulfate (PMS) with Co_3O_4–SnO_2/RSBC, Environmental Research, 187 (2020) 109665.
[12] Z. Wang, H. Jia, H. Zhao, R. Zhang, C. Zhang, K. Zhu, X. Guo, T. Wang, L. Zhu, Oxygen Limitation Accelerates Regeneration of Active Sites on a MnO_2 Surface: Promoting Transformation of Organic Matter and Carbon Preservation, Environmental Science & Technology, 56 (2022) 9806-9815.
[13] K. Wang, Q. Li, B. Liu, B. Cheng, W. Ho, J. Yu, Sulfur-doped g-C_3N_4 with enhanced photocatalytic CO_2-reduction performance, Applied Catalysis B: Environmental, 176-177 (2015) 44-52.
[14] H. Chen, Y. Xu, K. Zhu, H. Zhang, Understanding oxygen-deficient La_2CuO_4-δperovskite activated peroxymonosulfate for bisphenol A degradation: The role of localized electron within oxygen vacancy, Applied Catalysis B: Environmental, 284 (2021) 119732.
[15] F.W. Boyom-Tatchemo, F. Devred, G. Ndiffo-Yemeli, S. Laminsi, E.M. Gaigneaux, Plasma-induced redox reactions synthesis of nanosized α-, γ- and δ-MnO_2 catalysts for dye degradation, Applied Catalysis B: Environmental, 260 (2020) 118159.
[16] Z. Lu, Y. Luo, Y. Wang, Y. Gong, C. Li, X. Liu, L. Niu, S. Xu, Ammonia-induced ($11\bar{1}$) facet exposure of δ-MnO_2 with enhanced electrochemical reactivity for high-performance supercapacitor, Materials Chemistry and Physics, 276 (2022) 125351.
[17] K. Chen, D. Xue, Nanoscale surface engineering of cuprous oxide crystals: the function of chloride, Nanoscience and Nanotechnology Letters, 3 (2011) 383-388.
[18] J. Kim, J. Wang, D.C. Ashley, V.K. Sharma, C.-H. Huang, Enhanced Degradation of Micropollutants in a Peracetic Acid–Fe(III) System with Picolinic Acid, Environmental Science & Technology, 56 (2022) 4437-4446.

[19] J. Zhu, S. Wang, H. Li, J. Qian, L. Lv, B. Pan, Degradation of phosphonates in Co(II)/peroxymonosulfate process: Performance and mechanism, Water Research, 202 (2021) 117397.

[20] L. Hou, X. Li, Q. Yang, F. Chen, S. Wang, Y. Ma, Y. Wu, X. Zhu, X. Huang, D. Wang, Heterogeneous activation of peroxymonosulfate using Mn-Fe layered double hydroxide: Performance and mechanism for organic pollutant degradation, Science of The Total Environment, 663 (2019) 453-464.

[21] Y. Ruan, X. Jia, C. Wang, W. Zhen, X. Jiang, Mn–Fe layered double hydroxide nanosheets: a new photothermal nanocarrier for O_2-evolving phototherapy, Chemical Communications, 54 (2018) 11729-11732.

[22] H. Chi, J. Wang, H. Wang, S. Li, M. Yang, S. Bai, C. Li, X. Sun, Y. Zhao, Y.-F. Song, Super-Stable Mineralization of Ni^{2+} Ions from Wastewater using CaFe Layered Double Hydroxide, Advanced Functional Materials, 32 (2022) 2106645.

[23] D. Fang, J. Xie, H. Hu, H. Yang, F. He, Z. Fu, Identification of MnO_x species and Mn valence states in MnO_x/TiO_2 catalysts for low temperature SCR, Chemical Engineering Journal, 271 (2015) 23-30.

[24] K.L. Pickrahn, S.W. Park, Y. Gorlin, H.-B.-R. Lee, T.F. Jaramillo, S.F. Bent, Active MnO_x Electrocatalysts Prepared by Atomic Layer Deposition for Oxygen Evolution and Oxygen Reduction Reactions, Advanced Energy Materials, 2 (2012) 1269-1277.

[25] Y. Wu, Y. Yu, J.Z. Zhou, J. Liu, Y. Chi, Z.P. Xu, G. Qian, Effective removal of pyrophosphate by Ca–Fe–LDH and its mechanism, Chemical Engineering Journal, 179 (2012) 72-79.

[26] M. Szabados, A. Gácsi, Y. Gulyás, Z. Kónya, Á. Kukovecz, E. Csányi, I. Pálinkó, P. Sipos, Conventional or mechanochemically-aided intercalation of diclofenac and naproxen anions into the interlamellar space of CaFe-layered double hydroxides and their application as dermal drug delivery systems, Applied Clay Science, 212 (2021) 106233.

[27] W. Wang, Y. Liu, Y. Yue, H. Wang, G. Cheng, C. Gao, C. Chen, Y. Ai, Z. Chen, X. Wang, The Confined Interlayer Growth of Ultrathin Two-Dimensional Fe_3O_4 Nanosheets with Enriched Oxygen Vacancies for Peroxymonosulfate Activation, ACS Catalysis, 11 (2021) 11256-11265.

[28] C. Chen, M. Yan, Y. Li, Y. Hu, J. Chen, S. Wang, X.-L. Wu, X. Duan, Single-atom co sites confined in layered double hydroxide for selective generation of surface-bound radicals via peroxymonosulfate activation, Applied Catalysis B: Environmental, 340 (2024) 123218.

[29] D.T. Oyekunle, B. Wu, F. Luo, J. Ali, Z. Chen, Synergistic effects of Co and N doped on graphitic carbon as an in situ surface-bound radical generation for the rapid degradation of emerging contaminants, Chemical Engineering Journal, 421 (2021) 129818.

[30] L. Yin, J. Wei, Y. Qi, Z. Tu, R. Qu, C. Yan, Z. Wang, F. Zhu, Degradation of pentachlorophenol in peroxymonosulfate/heat system: Kinetics, mechanism, and theoretical calculations, Chemical Engineering Journal, 434 (2022) 134736.

[31] I. Othman, J. Hisham Zain, M. Abu Haija, F. Banat, Catalytic activation of peroxymonosulfate using $CeVO_4$ for phenol degradation: An insight into the reaction pathway, Applied Catalysis B: Environmental, 266 (2020) 118601.

[32] X. Zhou, M. Luo, C. Xie, H. Wang, J. Wang, Z. Chen, J. Xiao, Z. Chen, Tunable S doping from Co_3O_4 to Co_9S_8 for peroxymonosulfate activation: Distinguished Radical/Nonradical species and generation pathways, Applied Catalysis B: Environmental, 282 (2021) 119605.

[33] H. Zeng, H. Zhu, J. Deng, B. Liu, S. Zhou, Z. Shi, L. Deng, Tunable peroxymonosulfate activation by (−111) crystal plane exposed δ-MnO_2: Oxidant concentration induced intrinsic mechanisms transformation, Chemical Engineering Journal, 473 (2023) 145222.

[34] K. Yin, Y. Shang, D. Chen, B. Gao, Q. Yue, X. Xu, Redox potentials of pollutants determining the dominate oxidation pathways in manganese single-atom catalyst (Mn-SAC)/peroxymonosulfate system: Selective catalytic mechanisms for versatile pollutants, Applied Catalysis B: Environmental, 338 (2023) 123029.

[35] H. Zeng, H. Zhu, J. Deng, Z. Shi, H. Zhang, X. Li, L. Deng, New insight into peroxymonosulfate activation by CoAl-LDH derived CoOOH: Oxygen vacancies rather than Co species redox pairs induced process, Chemical Engineering Journal, 442 (2022) 136251.

[36] K. Yin, R. Wu, Y. Shang, D. Chen, Z. Wu, X. Wang, B. Gao, X. Xu, Microenvironment modulation of cobalt single-atom catalysts for boosting both radical oxidation and electron-transfer process in Fenton-like system, Applied Catalysis B: Environmental, 329 (2023) 122558.

[37] H. Zeng, L. Deng, H. Zhang, C. Zhou, Z. Shi, Development of oxygen vacancies enriched CoAl hydroxide@hydroxysulfide hollow flowers for peroxymonosulfate activation: A highly efficient singlet oxygen-dominated oxidation process for sulfamethoxazole degradation, Journal of Hazardous Materials, 400 (2020) 123297.

[38] K. Yin, L. Peng, D. Chen, S. Liu, Y. Zhang, B. Gao, K. Fu, Y. Shang, X. Xu, High-loading of well dispersed single-atom catalysts derived from Fe-rich marine algae for boosting Fenton-like reaction: Role identification of iron center and catalytic mechanisms, Applied Catalysis B: Environmental, 336 (2023) 122951.

[39] X. Li, X. Wen, J. Lang, Y. Wei, J. Miao, X. Zhang, B. Zhou, M. Long, P.J.J. Alvarez, L. Zhang, CoN_1O_2 Single-Atom Catalyst for Efficient Peroxymonosulfate Activation and Selective Cobalt(IV)=O Generation, Angewandte Chemie International Edition, 62 (2023) e202303267.

[40] L. Wu, Z. Sun, Y. Zhen, S. Zhu, C. Yang, J. Lu, Y. Tian, D. Zhong, J. Ma, Oxygen Vacancy-Induced Nonradical Degradation of Organics: Critical Trigger of Oxygen (O_2) in the Fe–Co LDH/Peroxymonosulfate System, Environmental Science & Technology, 55 (2021) 15400-15411.

[41] N. Jiang, H. Xu, L. Wang, J. Jiang, T. Zhang, Nonradical Oxidation of Pollutants with Single-Atom-Fe(III)-Activated Persulfate: Fe(V) Being the Possible Intermediate Oxidant, Environmental Science & Technology, 54 (2020) 14057-14065.

[42] K. Lin, W. Liu, J. Gan, Oxidative Removal of Bisphenol A by Manganese Dioxide: Efficacy, Products, and Pathways, Environmental Science & Technology, 43 (2009) 3860-3864.

[43] Y. Bao, C. Lian, K. Huang, H. Yu, W. Liu, J. Zhang, M. Xing, Generating High-valent

Iron-oxo ≡FeIV=O Complexes in Neutral Microenvironments through Peroxymonosulfate Activation by Zn−Fe Layered Double Hydroxides, Angewandte Chemie International Edition, 61 (2022) e202209542.

[44] Y. Gao, Z. Chen, Y. Zhu, T. Li, C. Hu, New Insights into the Generation of Singlet Oxygen in the Metal-Free Peroxymonosulfate Activation Process: Important Role of Electron-Deficient Carbon Atoms, Environmental Science & Technology, 54 (2020) 1232-1241.

[45] Y. Yang, P. Zhang, K. Hu, P. Zhou, Y. Wang, A.H. Asif, X. Duan, H. Sun, S. Wang, Crystallinity and valence states of manganese oxides in Fenton-like polymerization of phenolic pollutants for carbon recycling against degradation, Applied Catalysis B: Environmental, 315 (2022) 121593.

[46] J. Pan, B. Gao, P. Duan, K. Guo, M. Akram, X. Xu, Q. Yue, Y. Gao, Improving peroxymonosulfate activation by copper ion-saturated adsorbent-based single atom catalysts for the degradation of organic contaminants: electron-transfer mechanism and the key role of Cu single atoms, Journal of Materials Chemistry A, 9 (2021) 11604-11613.

[47] L.-S. Zhang, X.-H. Jiang, Z.-A. Zhong, L. Tian, Q. Sun, Y.-T. Cui, X. Lu, J.-P. Zou, S.-L. Luo, Carbon Nitride Supported High-Loading Fe Single-Atom Catalyst for Activation of Peroxymonosulfate to Generate $^1O_2$ with 100 % Selectivity, Angewandte Chemie International Edition, 60 (2021) 21751-21755.

[48] J. Zou, Y. Huang, L. Zhu, Z. Cui, B. Yuan, Multi-wavelength spectrophotometric measurement of persulfates using 2,2′-azino-bis(3-ethylbenzothiazoline-6-sulfonate) (ABTS) as indicator, Spectrochimica Acta Part A: Molecular and Biomolecular Spectroscopy, 216 (2019) 214-220.

[49] J. Du, J. Bao, Y. Liu, S.H. Kim, D.D. Dionysiou, Facile preparation of porous Mn/Fe_3O_4 cubes as peroxymonosulfate activating catalyst for effective bisphenol A degradation, Chemical Engineering Journal, (2018).

[50] H. Li, N. Yuan, J. Qian, B. Pan, Mn_2O_3 as an Electron Shuttle between Peroxymonosulfate and Organic Pollutants: The Dominant Role of Surface Reactive Mn(IV) Species, Environmental Science & Technology, 56 (2022) 4498-4506.

[51] L. Ai, S. Yang, W. Wei, Y. Li, X. Zheng, J. Jiang, Confinement of cobalt phosphides in nitrogen-doped carbon hosts for efficient peroxymonosulfate activation: Understanding charge-imbalance induced coordinative radical/non-radical oxidation, Separation and Purification Technology, 322 (2023) 124257.

[52] K.Z. Huang, H. Zhang, Direct Electron-Transfer-Based Peroxymonosulfate Activation by Iron-Doped Manganese Oxide (δ-MnO_2) and the Development of Galvanic Oxidation Processes (GOPs), Environmental Science & Technology, 53 (2019) 12610-12620.

[53] X. Yu, W. Qin, X. Yuan, L. Sun, F. Pan, D. Xia, Synergistic mechanism and degradation kinetics for atenolol elimination via integrated UV/ozone/peroxymonosulfate process, Journal of Hazardous Materials, 407 (2021) 124393.

[54] F.E. Scully, J. Hoigné, Rate constants for reactions of singlet oxygen with phenols and other compounds in water, Chemosphere, 16 (1987) 681-694.

[55] J. Zhang, C. Wang, N. Huang, M. Xiang, L. Jin, Z. Yang, S. Li, Z. Lu, C. Shi, B.

638 Cheng, H. Xie, H. Li, Humic acid promoted activation of peroxymonosulfate by Fe_3S_4 for
639 degradation of 2,4,6-trichlorophenol: An experimental and theoretical study, Journal of
640 Hazardous Materials, 434 (2022) 128913.
641 [56] A. Greer, Christopher Foote's Discovery of the Role of Singlet Oxygen [$^1O_2$ ($1\Delta g$)] in
642 Photosensitized Oxidation Reactions, Accounts of Chemical Research, 39 (2006) 797-804.

643

644

645 **Figures**

646

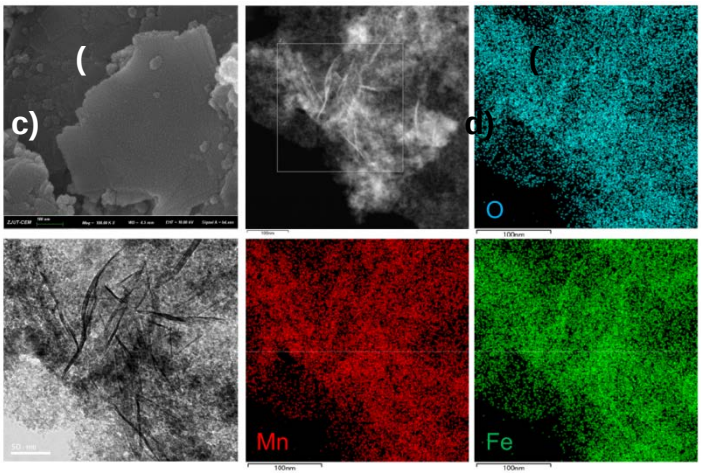

647

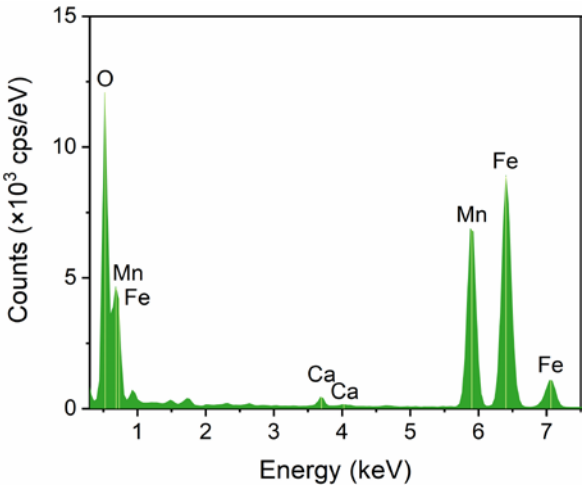

648

649 **Figure. 1.** (a) SEM, (b) HR-TEM, (c) EDS-mapping and (d) element analysis of MF-MnO_x.
650

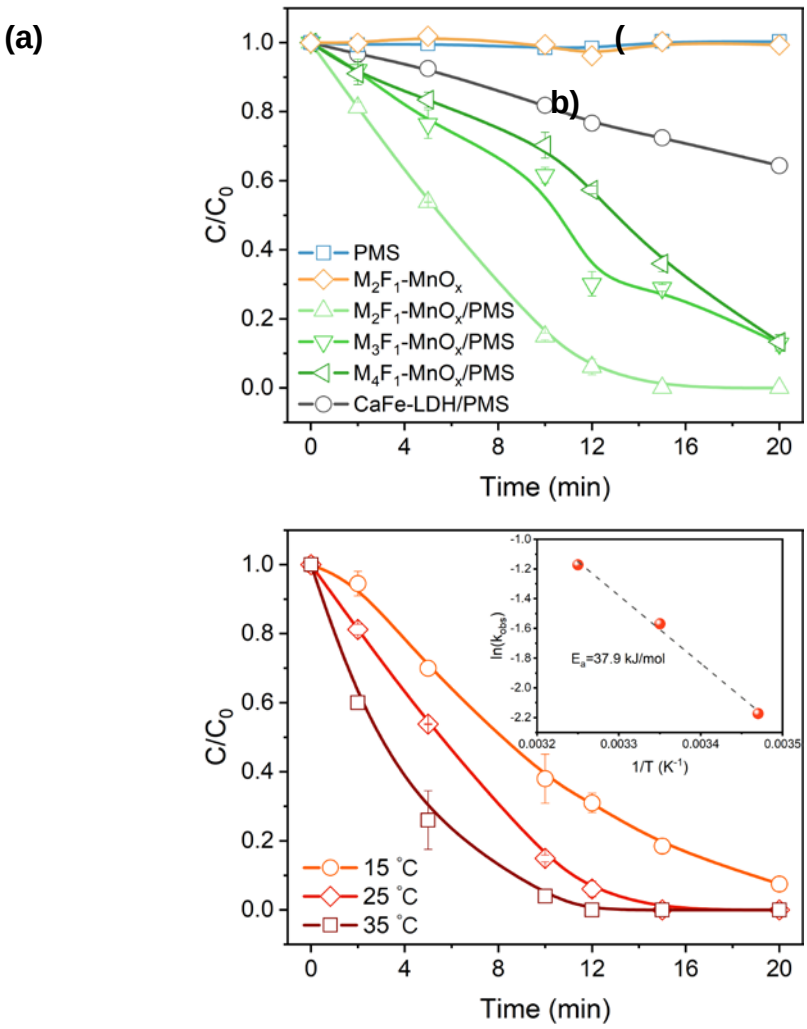

Figure. 2. (a) BPA degradation in different catalytic systems; (b) Effect of temperature on BPA degradation by MF-MnO_x/PMS system ([Catalyst] = 0.2 g/L, [PMS] = 0.2 mM, [BPA] = 5 mg/L).

658

(a)

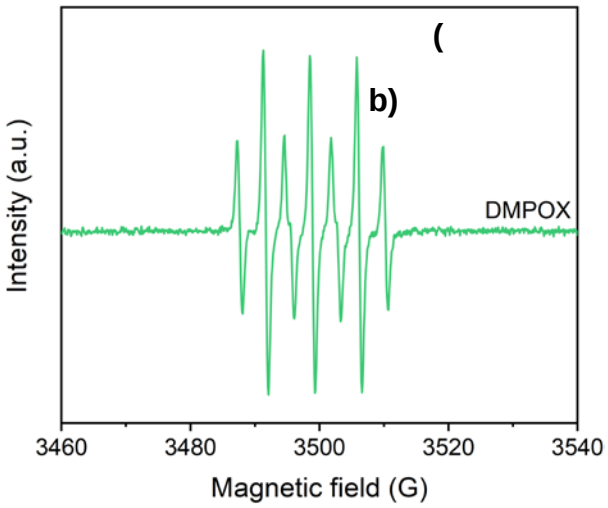

659

(c)

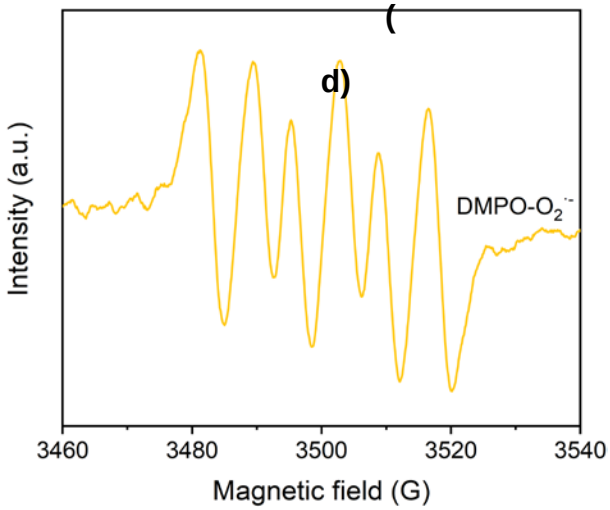

660

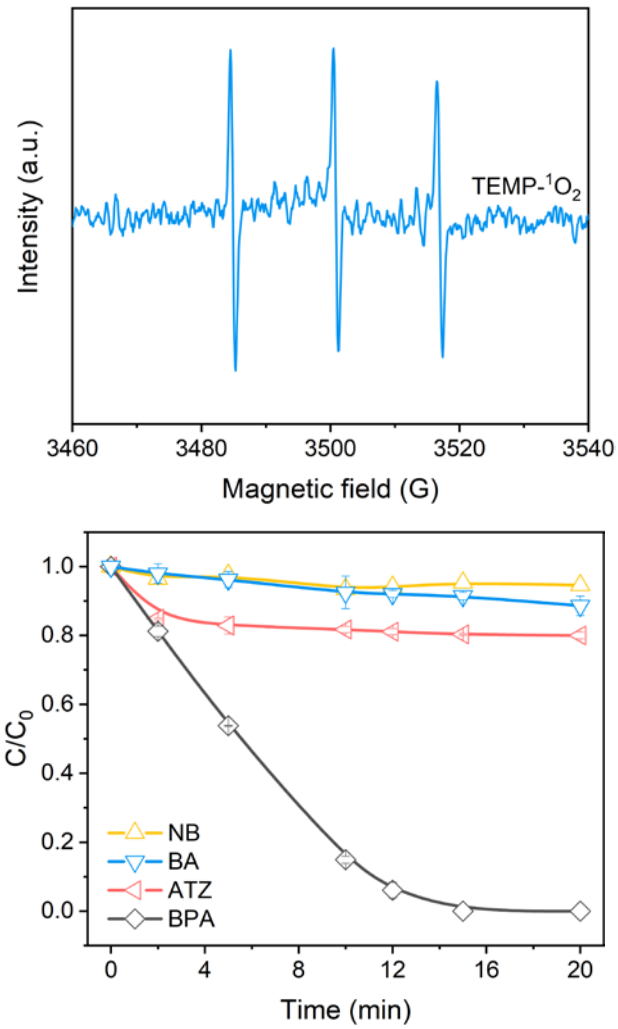

Figure. 3. (a) ESR spectra of DMPO-$SO_4^{\bullet-}$ and DMPO-$^{\bullet}OH$; (b) ESR spectra of DMPO-$O_2^{\bullet-}$; (c) ESR spectra of TEMP-$^1O_2$; (d) Removal of NB, BA, ATZ by MF-MnO_x/PMS system ([Catalyst] = 0.2 g/L, [PMS] = 0.2 mM, [Pollutant] = 5 mg/L).

668

(a)

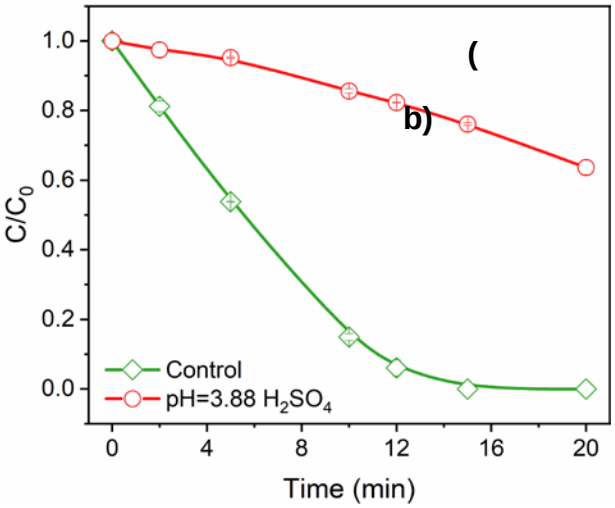

669

(c)

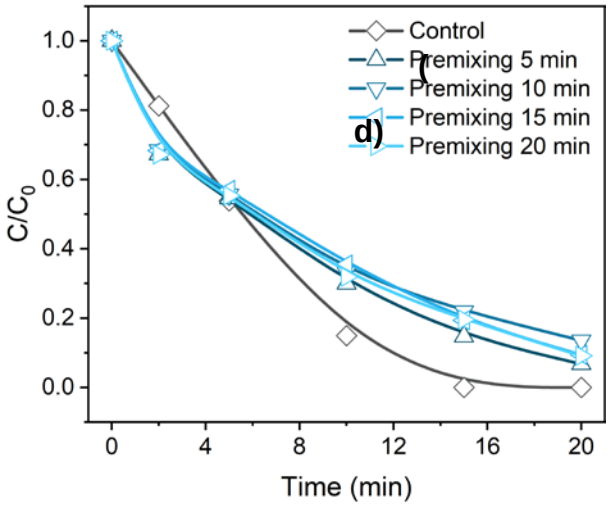

670

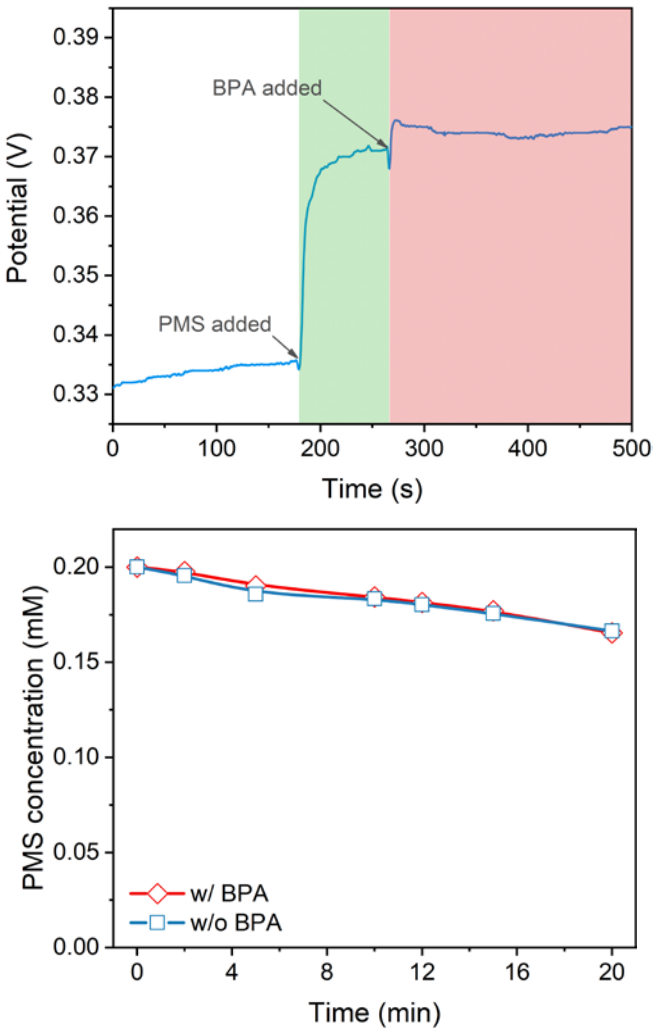

Figure. 4. (a) BPA degradation by MF-MnO_x/H_2SO_4 system at pH=3.88 (pH±0.2, [Catalyst] = 0.2 g/L, [BPA] = 5 mg/L); (b) Effect of premixing time on BPA degradation by MF-MnO_x/PMS system ([Catalyst] = 0.2 g/L, [PMS] = 0.2 mM, [BPA] = 5 mg/L); (c) The open-circuit potential variation in MF-MnO_x with the addition of PMS and BPA; (d) PMS consumption curves in MF-MnO_x/PMS system with/without BPA addition ([Catalyst] = 0.2 g/L, [PMS] = 0.2 mM, [BPA] = 5 mg/L).

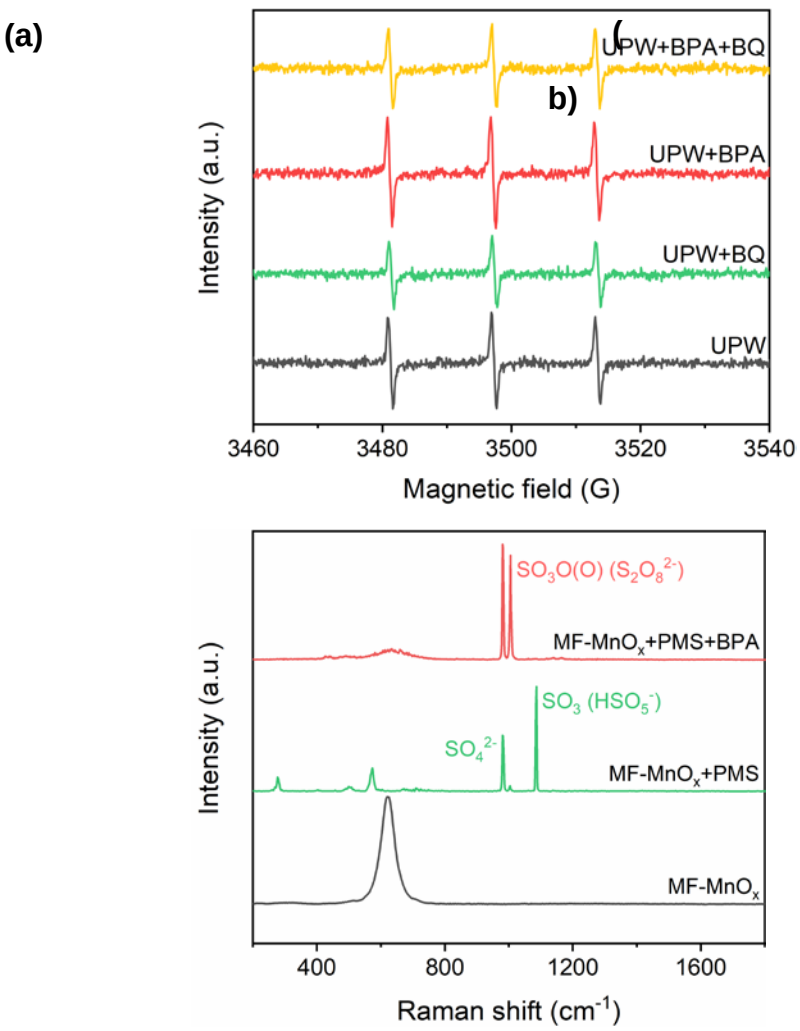

Figure. 5. (a) Quantitative ESR spectra of TEMP-$^1O_2$ in UPW, UPW+BQ, UPW+BPA, and UPW+BPA+BQ systems; (b) In situ-Raman spectra of MF-MnO_x, MF-MnO_x+PMS, and MF-MnO_x+PMS+BPA systems.

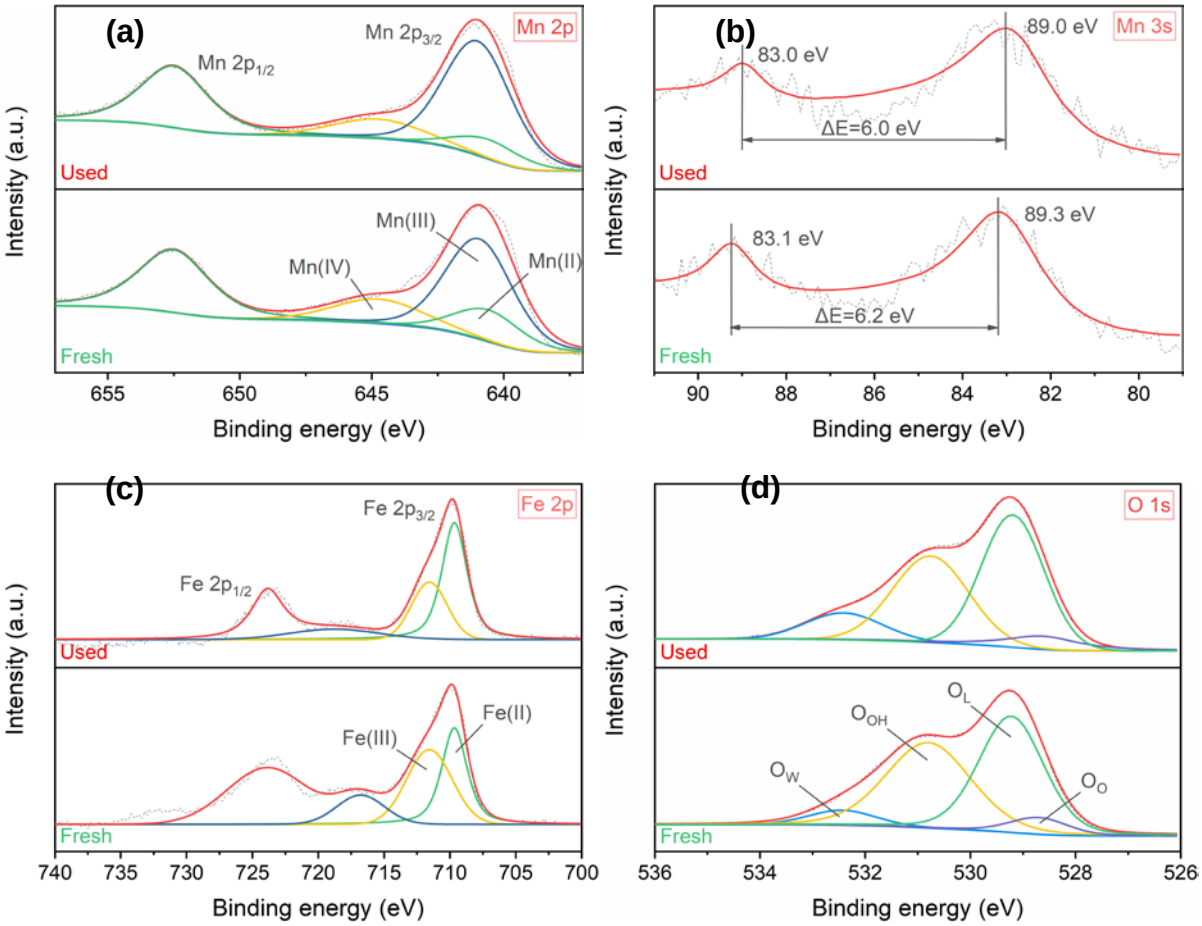

Figure. 6. XPS spectra of the fresh and used MF-MnO_x: (a) Mn 2p, (b) Mn 3s, (c) Fe 2p, (d) O 1s.

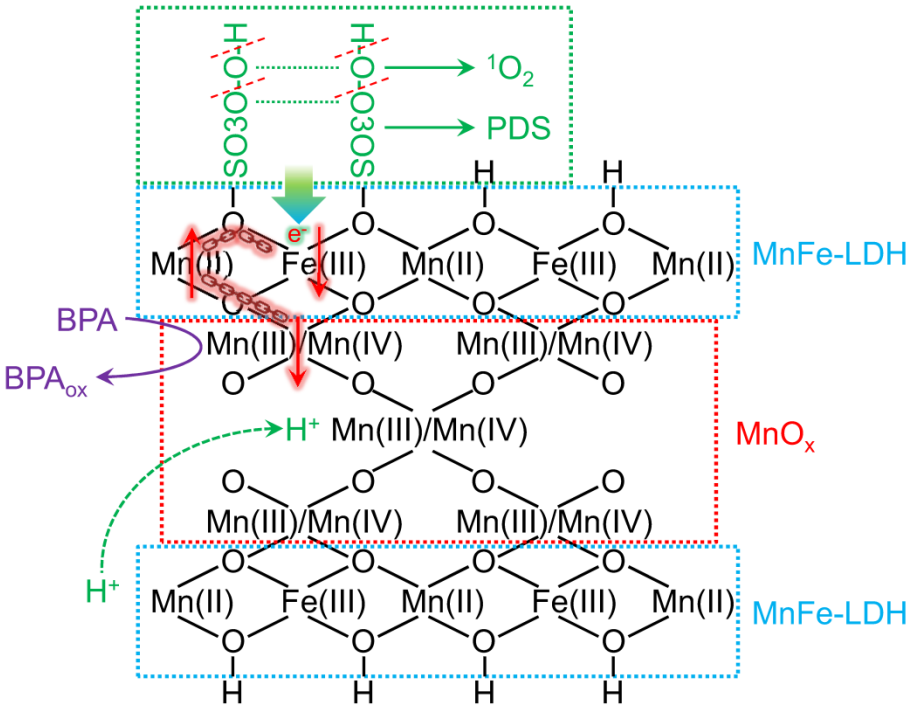

Figure. 7. Proposed mechanism of BPA degradation by MF-MnO_x/PMS system

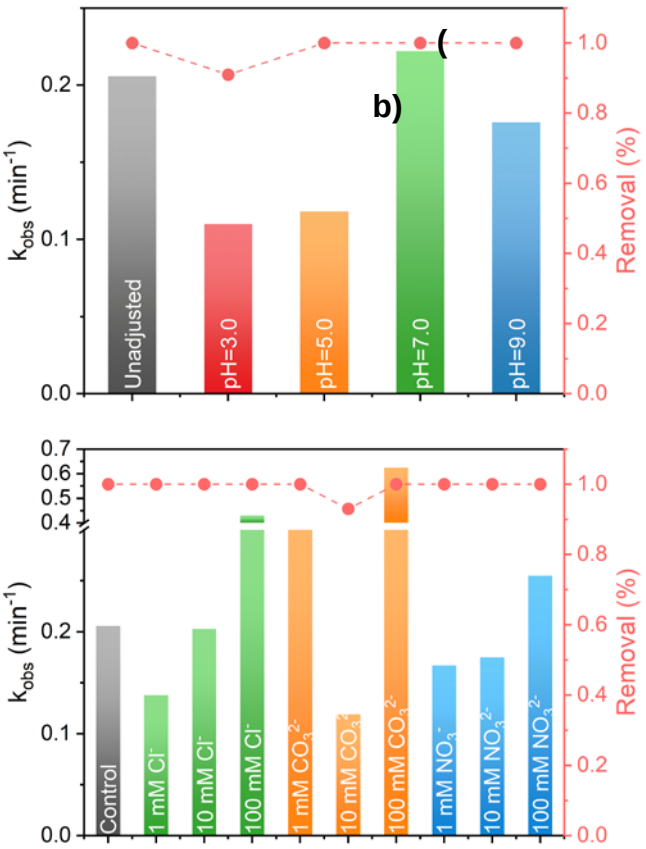

Figure. 8. Effect of (a) initial pH and (b) coexisting anions on BPA degradation by MF-MnO_x/PMS system ([Catalyst] = 0.2 g/L, [PMS] = 0.2 mM, [BPA] = 5 mg/L).